Tracking and measuring of clay shrinking and swelling using spaceborne remote sensing

André Burnol[1*], Michael Foumelis[1], Sébastien Gourdier[1], Jacques Deparis[1], Daniel Raucoules[1]
(1) BRGM, DRP, Orléans, France

Corresponding Author. Email : a.burnol@brgm.fr

Abstract

New capabilities for measuring and monitoring are needed to improve the shrink/swell hazard. A new French experimental site at Chaingy (Centre-Val de Loire) has been instrumented using extensometers at the surface and soil moisture sensors in the clay layer. Here we show by direct comparison between remote and *in situ* data for a period longer than three years that the vertical ground displacements are well-captured by the Multi-Temporal Synthetic Aperture Radar Interferometry (MT-InSAR) technique. In addition to the one-year period, two sub-annual periods that reflect both average ground shrinking and swelling timeframes are unraveled by a wavelet-based analysis. Moreover, we propose here to combine data from two satellite sensors, namely the surface soil moisture from the SMOS satellite with the vertical displacement from Sentinel-1A/1B. The relative phase difference between both time series for the shrinking and swelling periods is calculated for assessing the variations in terms of depth and thickness of the clay layer. An Electrical Resistivity Tomography (ERT) survey is carried out in the studied zone to validate this new method relying fully on remote sensing observations. With regard to future works, the same method coupling different satellites acquisitions may be scaled up to track the expansive clays in a larger area.

Introduction

Among the various natural risks in France, the risk due to shrinking and swelling of subsurface clays is the second most important cause of financial compensation from insurance companies behind the flooding risk. In 2010, the first global shrink/swell hazard map of metropolitan France, based on 1:50,000 geological maps, geotechnical data and spatial distribution of building damages is published by BRGM. So far, *in situ* monitoring of soil moisture/ground movements and *ex situ* clay characterization are the traditional way to study this risk, as carried out at the Mormoiron site with a Mediterranean climate (Vincent *et al.*, 2007a; Vincent *et al.*, 2007b). Standard ground displacement monitoring techniques (e.g. extensometers, GNSS) provide information on a very limited number of points within an area. Allowing a higher density of measurement points, the monitoring using Multi-Temporal Synthetic Aperture Radar Interferometry (MT-InSAR) techniques has been intensively developed in the last decades to track land subsidence or uplift related to groundwater extraction or recharge of aquifers around large cities (Declercq *et al.*, 2017; Foumelis *et al.*, 2016; Foumelis, 2012). Conversely, the monitoring of expansive clays using InSAR has been the subject of very few studies until now(Bonì *et al.*, 2018; Burnol *et al.*, 2019; Fryksten and Nilfouroushan, 2019). The major limiting factor to this purpose was the non-availability of relatively high-temporal resolution remote sensing datasets. There is indeed the requirement for fine temporal sampling due to the non-linear behaviour with respect to time of the shrink/swell cyclic behaviour (Raucoules *et al.*, 2009). The launch by the European Space Agency (ESA) of the Copernicus Sentinel-1A/1B satellites enables the systematic data provision, with a 6-day repeat cycle at the equator. Since 2016, a new site characterized by a high shrink/swell hazard level and located at Chaingy, an urban area with a semi-oceanic (i.e. slightly continental) climate, has been instrumented. Two *in situ* extensometers (EXT1 and EXT2), spaced about 12 m apart, and ten soil moisture sensors at 1.2 m depth are deployed in the studied zone (Fig. 1). Between September 2016 and

December 2019, the entire Sentinel-1A/1B archive data from both ascending and descending orbit geometries, 183 and 178 scenes, respectively, were processed using the CNR-IREA P-SBAS (Parallel Small BAseline Subset) service (F. Casu *et al.*, 2014; M. Manunta *et al.*, 2019) implemented on the Geohazards Exploitation Platform (GEP, https://geohazards-tep.eu) (Foumelis *et al.,* 2019). The temporal evolution of ground displacement is compared to the *in situ* measurements (Fig. 2). We provide evidence that MT-InSAR techniques, in our case the P-SBAS (provided at 90m x 90m spatial resolution), enable accurate measurement of the ground motion cycles due to the clay swelling and shrinking. Moreover, we compare the in-ground soil moistures to the surface soil moisture acquired by the SMOS satellite (Cabot, 2016). Finally, we propose a completely new method for evaluating the depth and the thickness of subsurface clay layers relying fully on remote sensing observations, namely the use of the relative phase difference between Sentinel-1 InSAR displacement and SMOS surface soil moisture time series. We use the electric tomography survey in order to validate this methodology in the studied zone.

Results and Discussion

Intercomparison of InSAR and *in situ* displacement time series

Displacements measured by InSAR are in the direction of the Line-of-Sight (LoS) of the satellite, while displacements measured by extensometers depict motion in the vertical direction. When exposed to moisture, the magnitude of the vertical expansion of soils will depend on the amount of expansive clay minerals in the subsurface. In addition, to the vertical displacement, the subsurface heterogeneities (i.e. clay depth, thickness and percentage of sand) may introduce spatial variability to the observed ground displacements. We assumed here that the interferometric method P-SBAS measures an average vertical displacement of the 90m x 90m cell and that all movements are taking place along the vertical direction. The InSAR LoS observations are independently projected to the vertical as well as combined to calculate the actual vertical motion component, using the ascending track (VERT-ASC), descending track (VERT-DES) and both tracks (VERT-ASC-DES) at the West Point (WP) (see method section). Qualitatively, there is a positive correlation between the vertical displacement VERT-ASC-DES at WP as calculated by InSAR using the satellite observations and as measured by ground-based extensometers EXT1 and EXT2 (Fig. 2a). Quantitatively, the least squares correlation coefficient (cc) is much higher for EXT2 (cc=0.69) than for EXT1 (cc=0.47). During the three-year period, the ground displacement time-series may be decomposed with the addition of a linear trend component T, a seasonal component S and an irregular residual component. There is a linear trend with a shrinking of about -2.2 mm/yr at EXT1 while the measured motion at EXT2 is merely a cyclic component with a shrinking of about -0.3 mm/yr (Fig. 2a). During the same period, the linear trend measured by Sentinel-1A/B lies between both values of EXT1 and EXT2 with a global shrinking of about -0.55 mm/yr . Concerning the cyclic part, the expansion is up to three times higher at EXT2 than at EXT1, with average swelling of 9.4 ± 2.0 mm and 3.1 ± 1.0 mm, respectively (Fig. 2a). Electrical resistive tomography has been carried out in

order to image the lithology stratification and the heterogeneity of the clay layer (i.e. depth, thickness, fraction of clay) (see method section). Along three 28.5 m long profiles in the WP cell (Fig. 1), the resistivity values range from 8 to 100 Ω.m and a three-layer stratified subsurface is highlighted (Fig. 3 and 4). We used two drill cores along the SC1-SC2 profile to define the clay subsurface material by the resistivity value (Long *et al.*, 2012) (Fig. 4 and Supplementary Fig. 3). A first layer above the depth of 0.59 m ± 0.22 m corresponds to topsoil and backfill with some clay lenses (Fig. 3 and 4). A second layer with a mean thickness of 1.5 m ± 0.42 m corresponds to the clay material with a resistivity lower than 17 Ω.m ± 1 Ω.m. Below 2.09 m ± 0.42 m, a third layer corresponds to sandy limestones with a resistivity gradient due to the weathering process. The depth (approx. at 0.5 m) and thickness (about 2.3 m) of the clay layer at EXT1 and EXT2 are very similar (Fig. 3b). However, the resistivity of the clay layer at EXT2 is much lower compared to EXT1, indicating that the clay fraction is much higher beneath EXT2 (Long *et al.*, 2012). That is also consistent with the expansion difference between the extensometers. Over the same period, the swelling magnitude measured by VERT-ASC-DES is 4.5 ± 0.5 mm that is within both extensometer values. This result in agreement with the assumption that the effect of the resolution of the remote sensing method using a 90 m x 90 m cell is an averaging of the vertical displacement in that cell.

Shrinking and swelling periods using Fourier power spectra and continuous wavelet transform

We use first the Fourier spectra of vertical displacements to calculate the main frequency components of time series of both extensometers as well as at WP and East Point (EP) cells of the P-SBAS grid (Fig. 5). The one-year seasonal period is found in the power spectrum of the four displacement times series at EXT1, EXT2, WP and EP (Fig. 6). In the frequency band between 2 and 4 yr^{-1} (corresponding to a period between 0.5 and 0.25 yr), there are three other frequencies which are noted F1, F21 and F22 (order of increasing frequency) and P1, P21 and P22 periods (order of decreasing period). It should be noted that the frequency values for all

displacement time series are close to the first three sub-annual components of the Fourier transform of the soil moistures E1 and W5 at 1.2 m depth (Fig. 6a) and the two ascending and descending time series of the surface soil moisture (SSM-ASC and SSM-DES) as measured by SMOS (Fig. 6b).

We use now the continuous wavelet power spectrum in order to unravel the intermittent physical mechanisms of the shrink/swell process (Fig 6). The continuous wavelet transform (CWT) tool permits the recognition of power in time-frequency space, along with assessing confidence levels against red noise backgrounds (see method section). September 2018 corresponds to the end of the shrinking period for EXT2 and WP cell (Fig. 2a) and there is a maximum of spectrum power at the P1 period (at 2 yr in Fig. 6). December 2017 corresponds to the start of the swelling period for EXT2 and there is a maximum of power at the P21 and P22 periods (at 1.25 yr in Fig. 6). Both swelling periods at WP cell are unraveled at different times, before 1.25 yr for P21 period and after 1.5 yr for P22 period. The same behaviour is observed at EXT1 extensometer and within EP cell (data not shown). In conclusion, the continuous wavelet transform highlights two sub-annual periods that reflect both average ground shrinking (P1) and swelling timeframes (P21).

Intercomparison of *in situ* soil moistures and SMOS satellite surface soil moistures

We investigated here the soil moisture variations acquired by E1 sensor (near EXT1, see Fig. 1) and W5 (near EXT2) that are both located at the same 1.2 m depth inside the clay layer (Fig. 3). The temporal variations of E1 and W5 are strongly correlated (cc = 0.73) during the three-year period (Fig. 2b). For the seasonal one-year period, there is a slight leading of E1 moisture relative to W5 (about 0.75 months) as calculated by the cross wavelet transform (XWT) (see method section). Indeed, the infiltration time of the meteoric water inside the clay layer at 1.2 m depth is lower in the E1 case, since the clay fraction of low permeability is shallower at EXT1 compared to EXT2.

We use here the term Surface Soil Moisture (SSM) to refer to the volumetric soil moisture in the first few centimeters (0-5 cm) of the soil. We investigated also the SSM acquired by the ascending (SSM-ASC) and descending (SSM-DES) orbits of the SMOS satellite, showing rather positive correlation (cc = 0.48). For the one-year period, SSM-ASC and SSM-DES are both in-phase and there is a slight leading of SSM-ASC relative to SSM-DES for the 5-month period (about 0.9 months) (Supplementary Fig. 2). Hence, the SSM-ASC dataset was considered more appropriate for calculating the phase differences to other time series in the following section. For the one-year period, the phase lead of the surface soil moisture SSM-ASC relative to the in-ground soil moistures E1 and W5 calculated by XWT is about 0.16 yr and 0.22 yr, respectively.

Estimating variations of expansive clay depth and thickness using the time series phase difference

The phase difference between the surface soil moisture (SSM) and InSAR displacement time series indicates the time lag between the cause and the effect in the shrink/swell process. We try to verify that depth and thickness of expansive clays are strongly linked to the phase difference between both time series for the shrinkage and swelling periods, respectively. We will use and compare the Fourier and XWT analyses to calculate this phase difference (see method section). The XWT spectra will be high in the time-frequency areas where both CWTs display high values, so this helps identify common time patterns in the two data sets. The XWT permits also the recognition of relative phase in time-frequency space (noted $\Delta\Phi$). While P1 and P21 are the shrinking and swelling periods found by the Fourier method (as described above), P1* and P21* are the same similar periods we found using XWT (Fig. 7 and 8). XWT tool will be used as well to calculate the circular standard deviation of this phase difference (see method section).

No significant difference is found between $\Delta\Phi$ values of both extensometers EXT1 and EXT2 for the shrinking period P1* and the swelling period P21* (Table 1). This result is consistent

with the tomography results which show that both depth and thickness of the clay is indeed comparable at the location of the extensometers (Fig. 3b). For the shrinking period P1*, the phase difference in degrees is three times higher at EXT2 ($\Delta\Phi = 107°$) than at WP ($\Delta\Phi = 34°$) (Table 1). This result for the shrinking period is further consistent with the tomographic findings indicating clays lenses in the first 0.5 m subsurface layer of the three 28m-wide profiles in the WP cell (Fig. 3 and 4). While there is no significant difference for the shrinking period, $\Delta\Phi$ is higher at EP cell ($\Delta\Phi = 110°$) in comparison to the WP cell ($\Delta\Phi = 72°$) for the swelling period (Table 1). This result is also consistent with the comparison by XWT of WP and EP ground displacement time series: both series are in phase for the shrinking period (about 0.5 year) while during the spring of the second year (2018), there is a slight leading of WP for the swelling period (0.25 yr) (arrows pointing down in Supplementary Figure 1b). One possible explanation of this result for the shrinking period is the presence of clay lenses in the first 0.5 m subsurface layer in the EP cell and for the swelling period the presence of deeper clays in the EP cell in comparison to the WP cell.

For the investigated site, we have shown how coupling SMOS surface soil moisture and Sentinel-1 InSAR displacement has enabled a new understanding of the heterogeneous behavior of the shrink/swell process. The relative phase difference as calculated by XWT with a standard deviation between both time series is used for assessing the variations in terms of depth and thickness of expansive clays. With regard to future works, the same method coupling different satellites acquisitions could be scaled up to track the expansive clays in a larger area and to estimate their relative depth and thickness.

Materials and Methods

Details about the methodologies implemented are given in the Supplementary information file.

Synthetic Aperture Radar (SAR) acquisitions. Copernicus Sentinel-1 mission data were utilized through the Geohazards Exploitation Platform (GEP), which provides access to various Earth Observation satellites repositories (incl. the Copernicus Open Access Hub, PEPS, CREODIAS, ASF and ONDA).

Interferometric SAR (InSAR) processing. The InSAR processing was performed using the Parallel Small Baseline Subset (P-SBAS) algorithm as implemented on the GEP. P-SBAS method is based on the processing of temporal series of co-registered SAR images acquired over the same target area for the generation of Line-of-Sight (LoS) ground displacement time series and velocity maps. The technique allows for the extraction of both linear and non-linear motion components without a priori assumption on the displacement model. Supposing a 1D vertical displacement, the LOS motions are projected to vertical, according to Equations 1-2, whereas combination of different viewing geometries provide us the actual vertical motion component (Equation 3, adapted from (Hanssen, 2001)).

$$VERT\_ASC = LOS_{ASC}/\cos\theta_{ASC} \qquad\qquad (1)$$
$$VERT\_DES = LOS_{DES}/\cos\theta_{DES} \qquad\qquad (2)$$
$$VERT\_ASC\_DES = (LOS_{ASC} + LOS_{DES})/(\cos\theta_{ASC} + \cos\theta_{DES}) \qquad (3)$$

VERT is the vertical displacement, LOS the motion in the Line-Of-Sight direction, θ the incidence angle, and the subscript ASC and DES for the ascending (θ_{ASC} = 34.4∘) and descending track (θ_{DES} = 42.8∘), respectively.

SMOS Level 3 Surface Soil Moisture (SSM) products. The SMOS Level 3 SSM products are downloaded through the CATDS dataset site (Cabot, 2016) (https://www.catds.fr). The data are presented over the Equal-Area Scalable Earth (EASE grid 2) (Brodzik *et al.*, 2012) with a sampling of about 25km x 25km and the studied area is included in one grid cell (Fig. 1). We use these 3-day aggregated SMOS-CATDS SSM products for ascending and descending overpasses between September 2016 and December 2019 for each Sentinel-1 acquisition (6 day-repeat cycle).

Signal processing using Fourier analysis. To perform filtering of satellite and *in situ* signals, time series of measurements are smoothed using a one-dimensional convolution approach with a HANNING window. To carry out the spectral analysis, the filtered time series is first padded with trailing zeros to a length of 100 yr before computing the discrete Fourier transform (DFT) using the fast Fourier transform (FFT) Matlab function. The frequency maxima of Fourier power spectrum are therefore computed with a precision of 1/100 yr^{-1}. The magnitude and the phase angles of complex FFT values are calculated by Matlab ABS and ANGLE operators, respectively. Whenever the jump between consecutive angles is greater than or equal to π radians, UNWRAP function shifts the angles by adding multiples of ±2π until the jump is less than π.

Signal processing using wavelet analysis. The wavelet transform is especially suited to extract features from low signal-to-noise ratio time-series and to identify localized intermittent periodicities. The Morlet wavelet is adapted to geophysical time series as described by (Torrence and Compo, 1998) who developed the software provided at http://paos.colorado.edu/research/wavelets. We used the Matlab version as adapted by (Grinsted *et al.*, 2004) and provided at http://www.glaciology.net/wavelet-coherence. The continuous wavelet power spectrum CWT expands time-series records into time/frequency space. The time-series input data must be equally spaced in time. Although Copernicus satellites have a regular revisit interval (6 days for Sentinel-1A/B and 3 days for SMOS), some

acquisitions may be missing or excluded from processing. These missing values are linearly interpolated using a constant time interval. The other time-series data of extensometers and soil moistures sensors are down-sampled using the same time interval. Two individual CWTs can be combined by using the cross wavelet transform (XWT) tool which is computed by multiplying the CWT of one time-series by the complex conjugate of the CWT of the second time-series. XWT image is the 2-D representation of the absolute value and the phase of the complex number in the time-frequency space. For many geophysical phenomena, an appropriate background spectrum is red noise (increasing power with decreasing frequency). ANGLEMEAN function calculates the mean angle found by XWT during a time period and the sigma which corresponds to a standard deviation.

Clay layer characterization using electric method. The data were collected using the IRIS Syscal Pro Plus multi-electrode imaging system with internal multiplexer. Three profiles were acquired using 96 stainless electrodes spaced every 30 cm. Length of the profile was 28.5 m. The measurement was carried out using Dipole-Dipole and Wenner configuration Due to good coupling, no data was removed during pre-processing. Inversion will be carried out using Res2DINV software with a L1 regulation norm. Root means square values was lower than 1% after fives iterations for the three profiles.

References

Bonì, R., Bosino, A., Meisina, C., Novellino, A., Bateson, L., and McCormack, H. (2018). A methodology to detect and characterize uplift phenomena in urban areas using Sentinel-1 data *Remote Sensing* 10, 607.

Brodzik, M. J., Billingsley, B., Haran, T., Raup, B., and Savoie, M. H. (2012). EASE-Grid 2.0: Incremental but Significant Improvements for Earth-Gridded Data Sets *ISPRS International Journal of Geo-Information* 1

Burnol, A., Aochi, H., Raucoules, D., Veloso, F. M. L., Koudogbo, F. N., Fumagalli, A., et al. (2019). Wavelet-based analysis of ground deformation coupling satellite acquisitions (Sentinel-1, SMOS) and data from shallow and deep wells in Southwestern France *Scientific Reports* 9, 8812.

Cabot, F. (2016). CATDS-PDC L3SM Aggregated - 3-day, 10-day and monthly global map of soil moisture values from SMOS satellite doi: https://doi.org/10.12770/b57e0d3d-e6e4-4615-b2ba-6feb7166e0e6

Declercq, P., Walstra, J., Gérard, P., Pirard, E., Perissin, D., Meyvis, B., et al. (2017). A Study of Ground Movements in Brussels (Belgium) Monitored by Persistent Scatterer Interferometry over a 25-Year Period *Geosciences* 7, 115.

F. Casu, S. Elefante, P. Imperatore, I. Zinno, M. Manunta, C. De Luca, et al. (2014). SBAS-DInSAR Parallel Processing for Deformation Time-Series Computation *IEEE Journal of Selected Topics in Applied Earth Observations and Remote Sensing* 7, 3285-3296

Foumelis, M. (2012). "Human induced groundwater level declination and physical rebound in northern Athens Basin (Greece) observed by multi-reference DInSAR techniques," in *IEEE International Geoscience and Remote Sensing Symposium, Munich, Germany, 22-27 July 2012, 820-823.* doi:10.1109/IGARSS.2012.6351436

Foumelis, M., Papadopoulou, T., Bally, P., Pacini, F., Provost, F., and Patruno, J. (2019). "Monitoring Geohazards Using On-Demand And Systematic Services On ESA's Geohazards Exploitation Platform," in *IGARSS 2019-2019 IEEE International Geoscience and Remote Sensing Symposium, Yokohama, Japan, Japan, 28 July-2 Aug. 2019, 5457-5460.* doi:10.1109/IGARSS.2019.8898304

Foumelis, M., Papageorgiou, E., and Stamatopoulos, C. (2016). Episodic ground deformation signals in Thessaly Plain (Greece) revealed by data mining of SAR interferometry time series *Int. J. Remote Sens.* 37, 3696-3711.

Fryksten, J. and Nilfouroushan, F. (2019). Analysis of Clay-Induced Land Subsidence in Uppsala City Using Sentinel-1 SAR Data and Precise Leveling *Remote Sensing* 11

Grinsted, A., Moore, J. C., and Jevrejeva, S. (2004). Application of the cross wavelet transform and wavelet coherence to geophysical time series *Nonlinear processes in geophysics* 11, 561-566.

Hanssen, R. F. (2001). *Radar interferometry: data interpretation and error analysis*. New York, Boston, Dordrecht, London, Moscow: Springer Science & Business Media.

Long, M., Donohue, S., L'Heureux, J., Solberg, I., Ronning, J. S., Limacher, R., et al. (2012). Relationship between electrical resistivity and basic geotechnical parameters for marine clays *Canadian Geotechnical Journal* 49, 1158-1168.

M. Manunta, C. De Luca, I. Zinno, F. Casu, M. Manzo, M. Bonano, et al. (2019). The Parallel SBAS Approach for Sentinel-1 Interferometric Wide Swath Deformation Time-Series Generation: Algorithm Description and Products Quality Assessment *IEEE Transactions on Geoscience and Remote Sensing* 57, 6259-6281

Raucoules, D., Bourgine, B., De Michele, M., Le Cozannet, G., Closset, L., Bremmer, C., et al. (2009). Validation and intercomparison of Persistent Scatterers Interferometry: PSIC4 project results *J. Appl. Geophys.* 68, 335-347.

Torrence, C. and Compo, G. P. (1998). A practical guide to wavelet analysis *Bull. Am. Meteorol. Soc.* 79, 61-78.

Vincent, M., Le Roy, S., Dubus, I., & Surdyk, N. (2007a). Experimental monitoring of water content and vertical displacements in clayey soils exposed to shrinking and swelling. *Revue Française de Géotechnique,* (120-121), 45-58.

Vincent, M., Plat, E., and Le Roy, S. (2007b). Cartographie de l'aléa retrait-gonflement et plans de prévention des risques *Revue française de géotechnique*, 189-200.

Acknowledgments

Authors contributions

A.B. conceived the study, wrote the main manuscript, prepared the figures 1-2 and 5-8, the table 1, performed the SMOS data, the wavelet-based analysis and provided the overall interpretation. M.F. performed the overall SAR data processing, prepared the Supplementary table 1. J.D. performed the electrical tomography, prepared the figures 3 and 4. S.G. conceived the experimental Chaingy site, performed the extensometers and soil moistures data processing and prepared the Supplementary figure 3. D.R. contributed to the interpretation of the SAR data and to the overall interpretation. All authors contributed to the text and reviewed the manuscript.
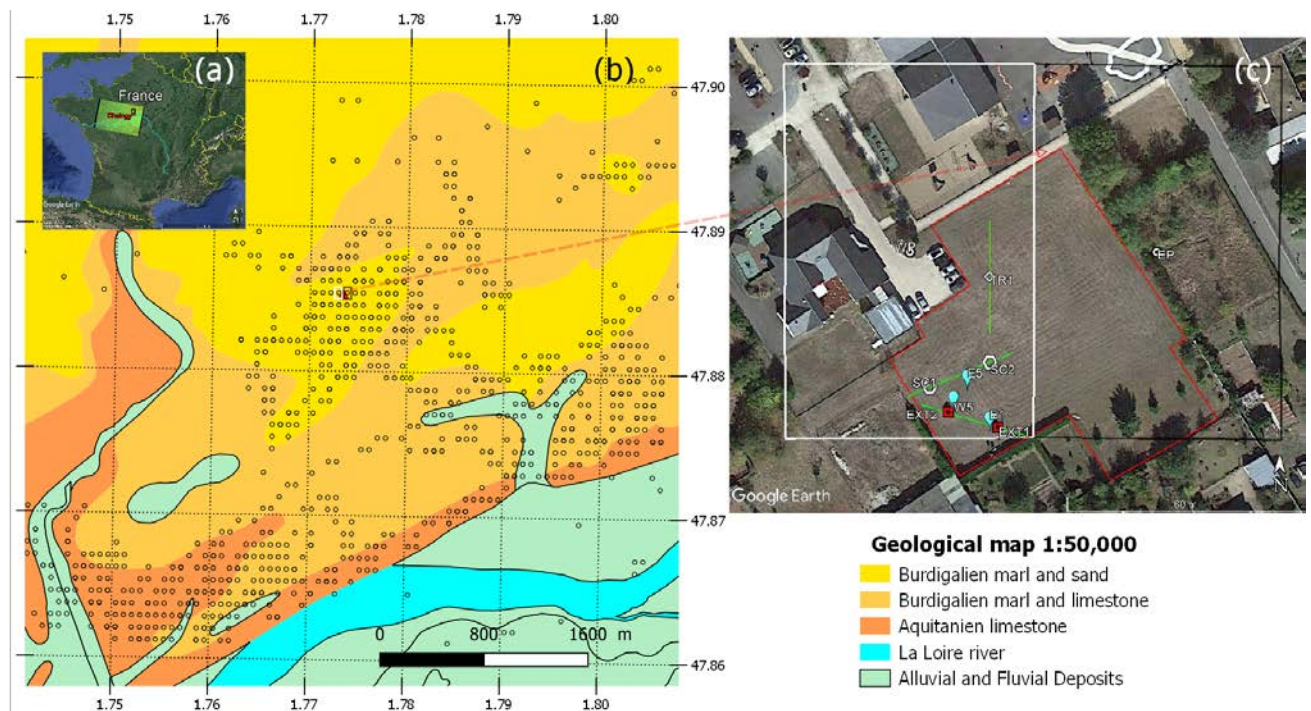
Figure 1: Map of the Chaingy experimental site. (a) Regional setting in France (Map data: Google, Landsat/Copernicus, SIO, NOAA, US Navy, NGA, GEBCO) that contains modified Copernicus Sentinel data (2016) and a ~25 km cell of the EASE equal-area grid used by the SMOS satellite (black rectangle). (b) Simplified superficial geology of the studied zone modified from the BRGM geological map of France at the 1:50,000 scale showing the P-SBAS grid (black circles) and the location of the studied zone (red filled polygon). (c) Details of the studied zone (red polygon) showing two extensometers (EXT1, EXT2) (red placemark), three soil moistures sensors at E1, E5 and W5 (blue placemark), three electric profiles (green line), two core sampling SC1 and SC2 (white polygon), two P-SBAS grid cells (white and black rectangles) around two grid points West Point WP and East Point EP (white circles). Maps a-c were created using Google Earth Pro and map b by QGIS (Version 2.18.0, http://qgis.org).
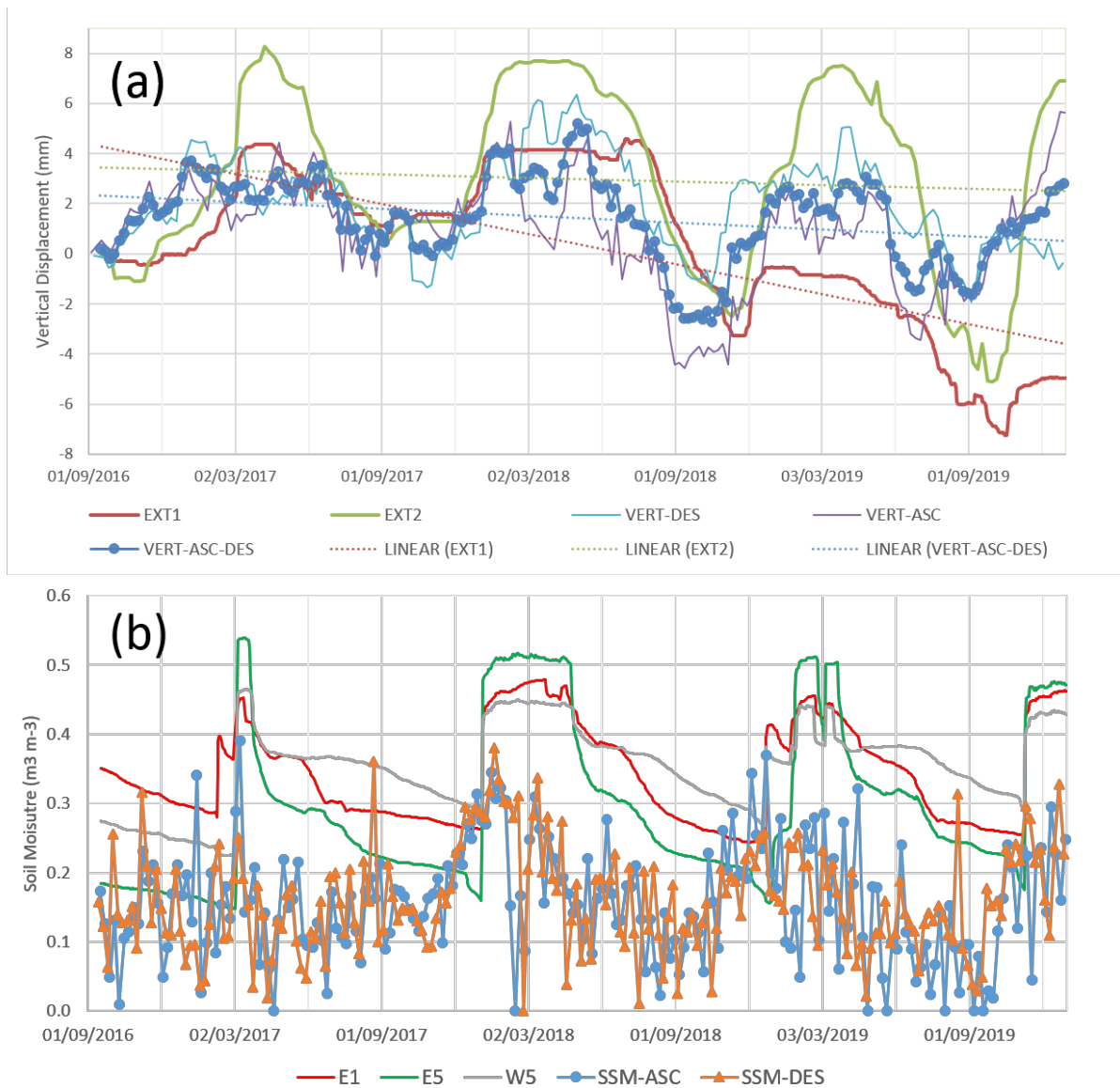
Figure 2: (a) Comparison of the vertical displacement of both extensometers (EXT1, EXT2) to three P-SBAS results: VERT-ASC using the ascending track, VERT-DES using the descending track and VERT-ASC-DES using both tracks of Sentinel-1 at West Point (WP). (b) Comparison of three soil moistures at about 1.2 m depth (E1, E5, W5) to the Surface Soil Moisture SSM-ASC and SSM-DES using the SMOS ascending and descending track, respectively.
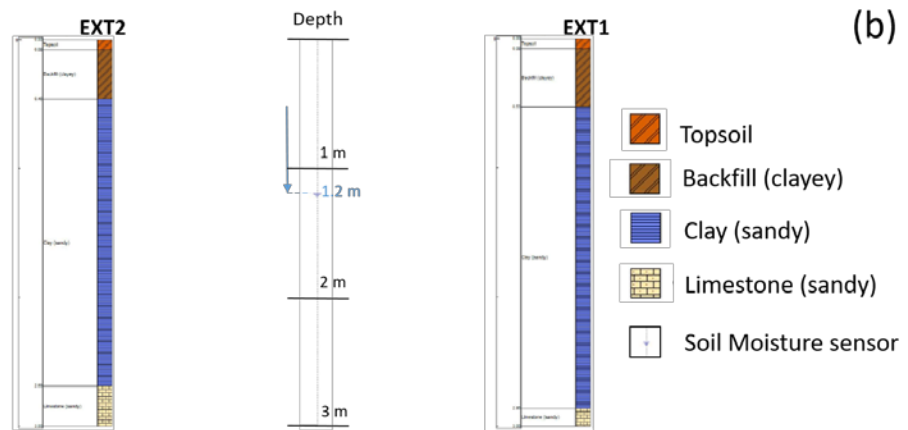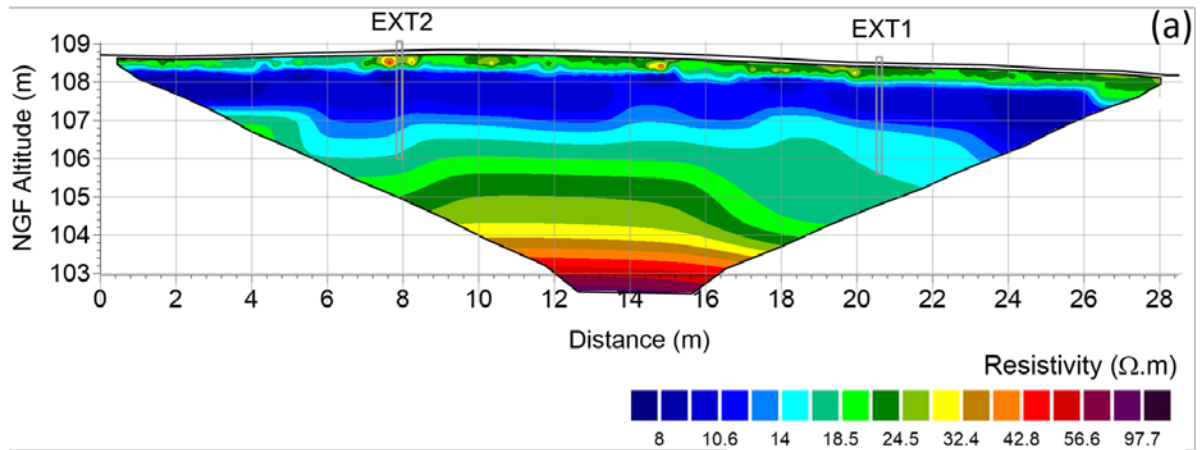
Figure 3: (a) Vertical cross section of resistivity along EXT1-EXT2 profile. (b) Clay depth and thickness at EXT1 and EXT2 deduced from the resistivity profile (see text).
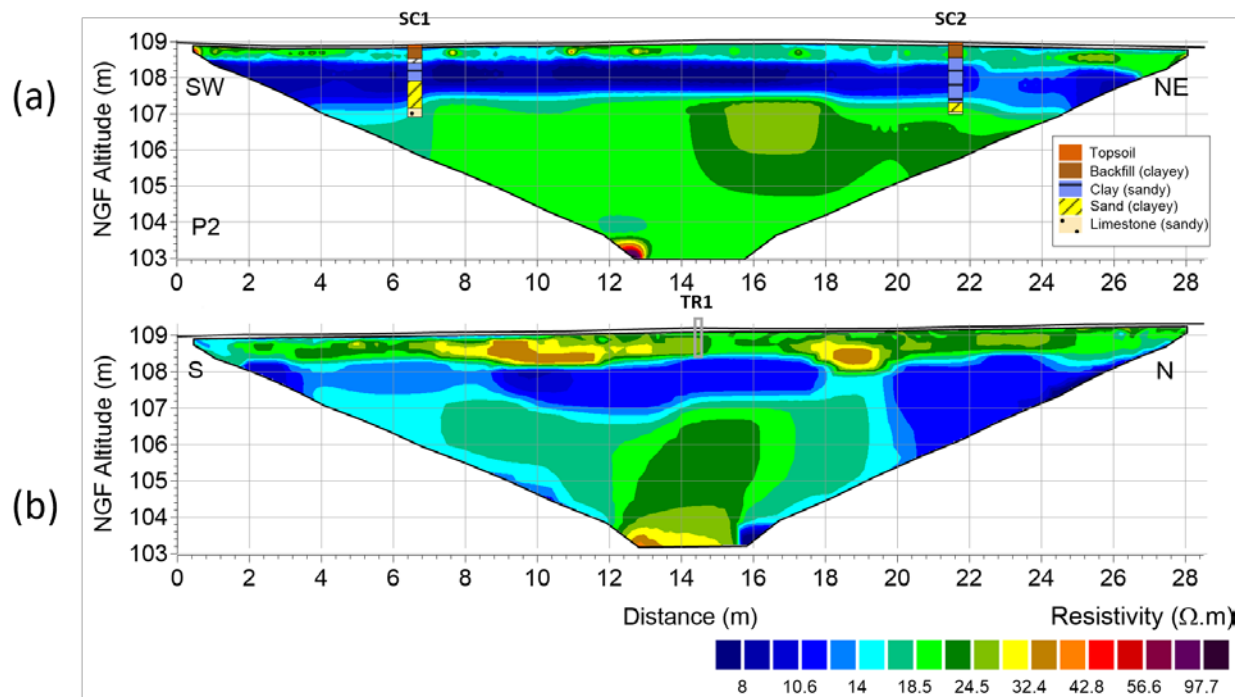
Figure 4: (a) Vertical cross section of resistivity along SC1-SC2 profile showing the SC1 and SC2 geological logs (see Supplementary File). (b) Vertical cross section of resistivity along South-North profile showing TR1 drilling.
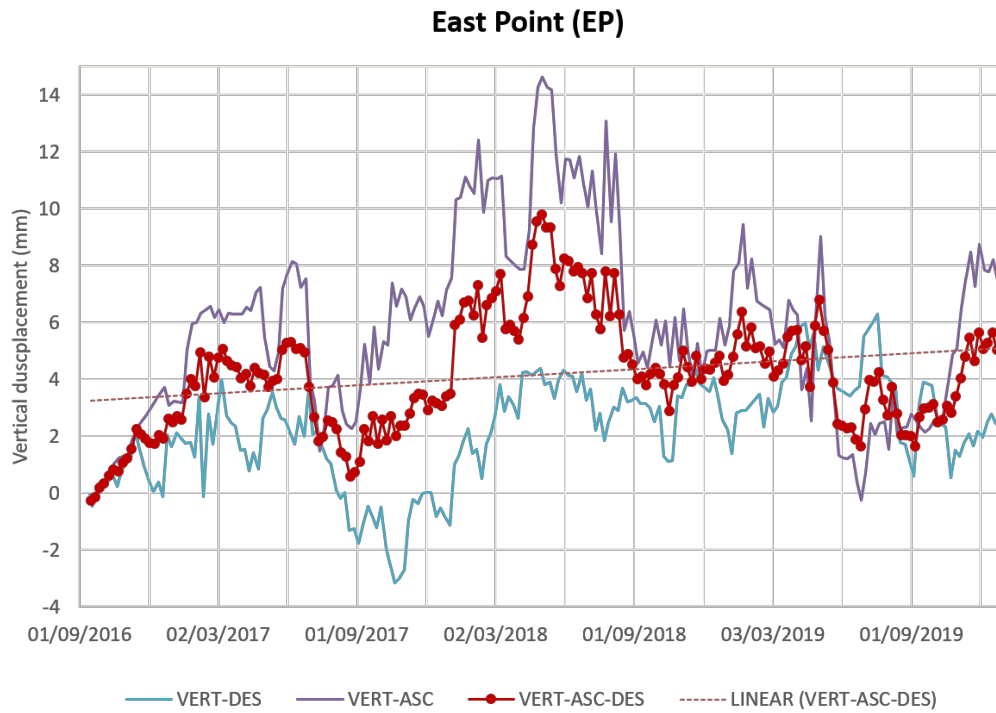
Figure 5: Comparison of three P-SBAS results: VERT-ASC using the ascending track, VERT-DES using the descending track and VERT-ASC-DES using both tracks of Sentinel-1 at East Point (EP).
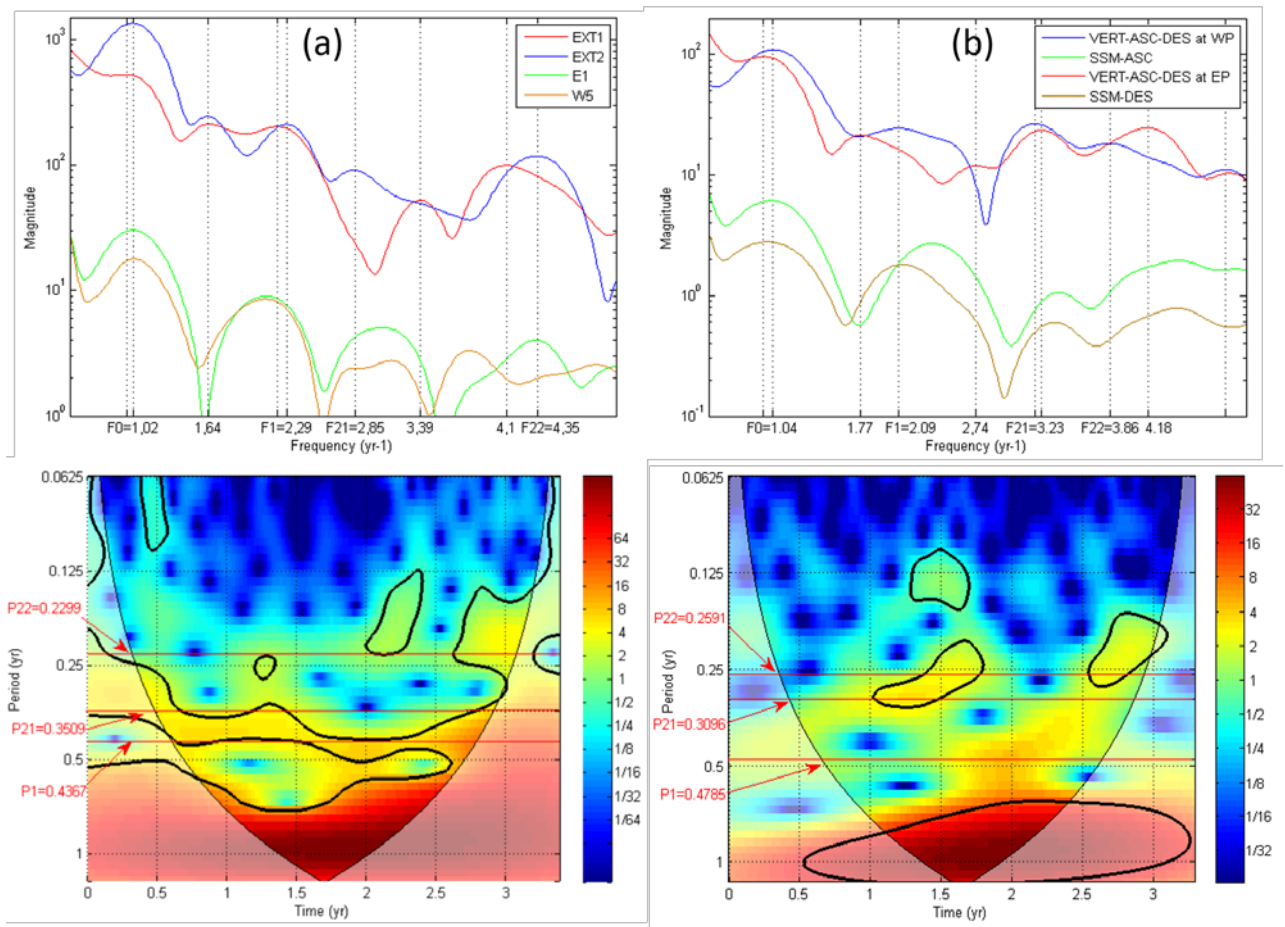
Figure 6: In the top, the magnitude of the Fast Fourier Transform (FFT) of different time series between 0.5 and 5 year-1 are shown: (a) vertical displacement of both extensometers (EXT1, EXT2) and the Soil Moisture at E1 and W5 (about 1.2 m depth), (b) VERT-ASC-DES for vertical displacement using ascending and descending S-1A/1B tracks at West Point (WP) and East Point (EP), SSM-ASC and SSM-DES for the Surface Soil Moisture using the ascending and descending SMOS track, respectively. In the bottom, the continuous wavelet transform (CWT) during 3.3 years (September 2016 – December 2020) are shown for two vertical displacements: (a) EXT2, (b) VERT-ASC-DES at WP. The thick contour designates the 5 % significant level against red noise (see method section). The cone of influence (COI) where edge effects might distort the picture is shown as a lighter shadow.
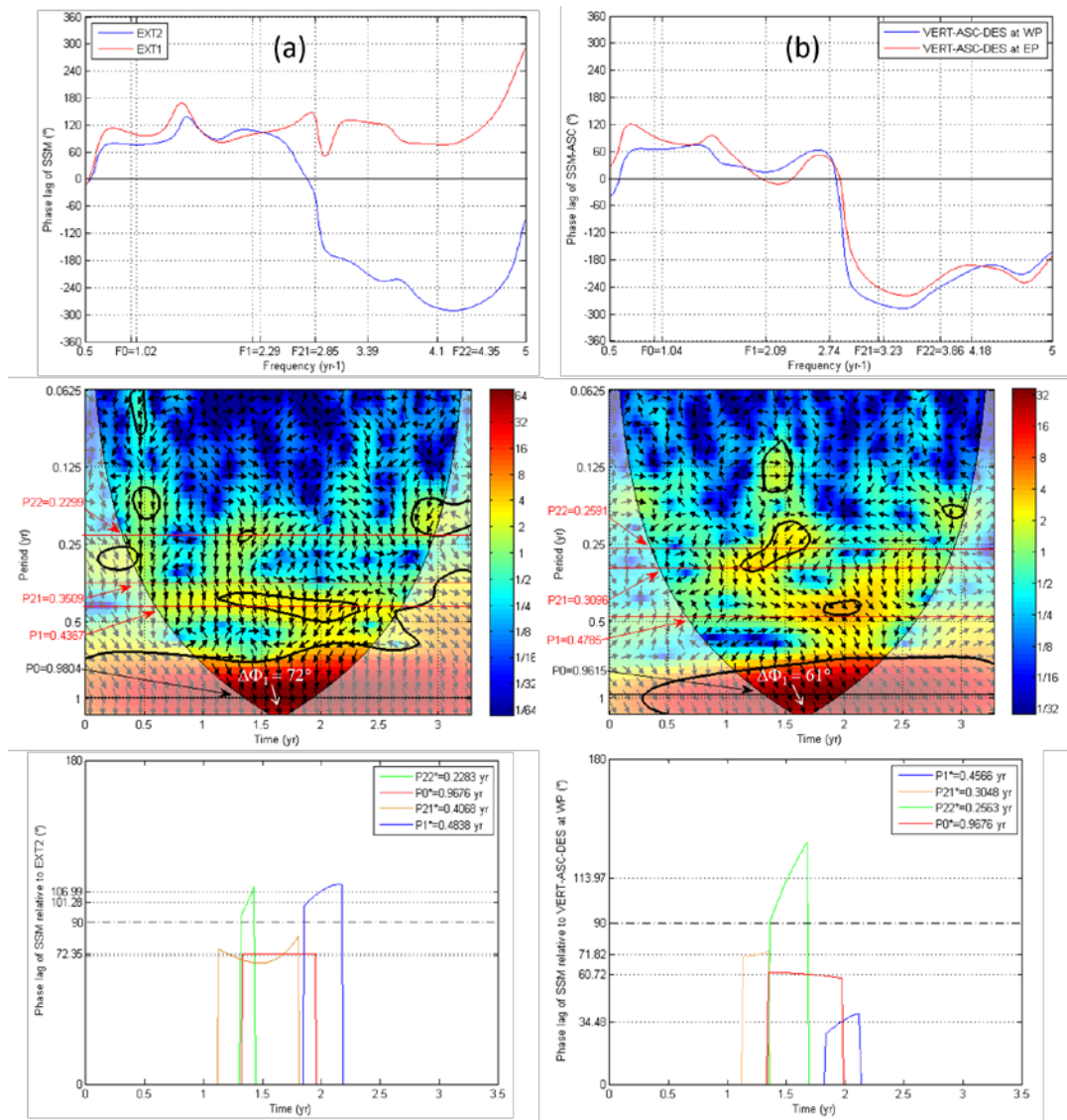
Figure 7: In the top, the phase angle difference in degrees between the FFT of the SSM-ASC using SMOS ascending track and the FFT of the displacement of four time series are shown: (a) EXT1 and EXT2, (b) VERT-ASC-DES at WP and EP. In the middle, the cross wavelet transform (XWT) between SSM-ASC and two times series is shown: (a) EXT2, (b) VERT-ASC-DES at WP. The relative phase relationship is shown as arrows, with in-phase pointing right and anti-phase pointing left and the Surface Soil Moisture leading by 90° pointing straight down. The cone of influence (COI) where edge effects might distort the picture is shown as a lighter shadow. In the bottom, the phase lags of SSM-ASC relative to the same times series are shown for the shrinking (P1*) and swelling (P21*, P22*) periods found using the thick contours of XWT that designate the 5 % significant level against red noise.
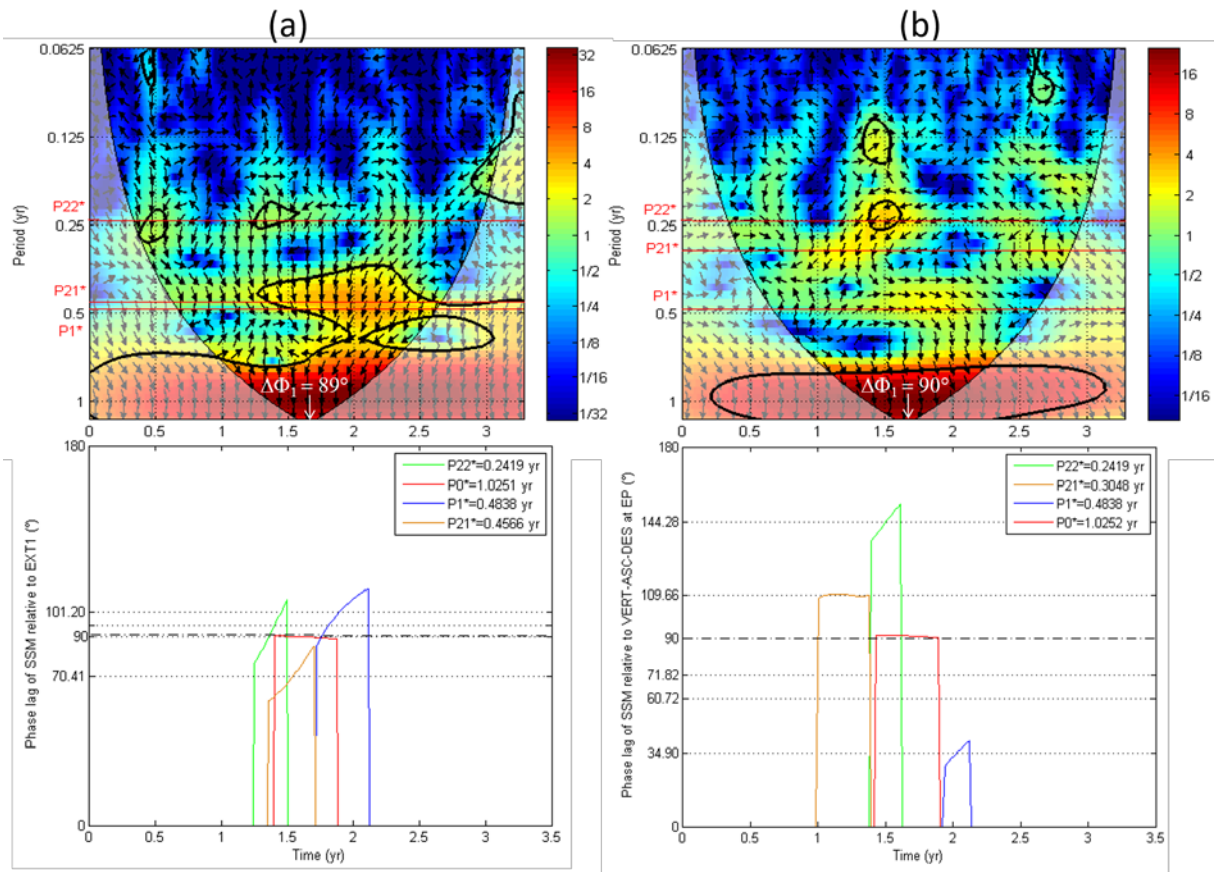
Figure 8: In the top, the cross wavelet transform (XWT) between SSM-ASC using SMOS ascending track and two times series is shown: (a) EXT1, (b) VERT-ASC-DES at East Point (EP). The relative phase relationship is shown as arrows, with in-phase pointing right and anti-phase pointing left and the Surface Soil Moisture leading by 90° pointing straight down. The cone of influence (COI) where edge effects might distort the picture is shown as a lighter shadow. In the bottom, the phase lags of SSM-ASC relative to the same times series are shown for the shrinking (P1*) and the swelling (P21*, P22*) periods.

Table 1: Comparison of Fourier FFT and cross-wavelet XWT analysis of phase angles and time lags of the surface soil moisture (SSM-ASC) relative to the vertical displacement at EXT1, EXT2, West Point (WP) cell and East Point (EP) cell for the seasonal (P0), shrinking (P1) and swelling (P21,P22) periods

	1-year period (P0)		Shrinking period (P1)		Swelling first period (P21)		Swelling second period (P22)		ΔΦ ∑ P1,P2
	Angle (°)	*Time (mth)*	*Angle (°)*	*Time (mth)*	*Angle (°)*	*Time (mth)*	*Angle (°)*	*Time (mth)*	*Time (mth)*
FFT at EXT1	102.0	**3.51**	99.63	1.50	125.86	1.24	77.25	0.63	**3.37**
XWT at EXT1	89.09	**3.04**	101.20	1.63	70.41	1.07	94.82	0.76	**2.70[§]**
	± 0.4	**± 0.01**	± 7.94	± 0.13	± 7.95	± 0.12	± 9.78	± 0.08	**± 0.25[§]**
FFT at EXT2	76.76	**2.51**	105.09	1.53	-38.69	0.45	70.76	0.54	**2.52**
XWT at EXT2	72.35	**2.33**	106.99	1.73	71.13	0.96	101.28	0.77	**2.69[§]**
	± 0.02	**± 0.00**	± 3.68	± 0.06	± 3.76	± 0.05	± 5.02	± 0.04	**± 0.11[§]**
FFT at WP cell	64.75	**2.08**	14.68	0.23	83.81	0.86	119.70	1.03	**2.13**
XWT at WP cell	60.72	**1.96**	34.48	0.52	71.82	0.73	113.97	0.97	**2.22**
	± 0.96	**± 0.03**	± 3.40	± 0.05	± 0.98	± 0.01	± 13.30	± 0.11	**± 0.18**
FFT at EP cell	92.16	**3.20**	42.85	0.52	112.48	1.14	168.36	1.34	**3.00**
XWT at EP cell	90.10	**3.08**	34.90	0.56	109.66	1.11	144.28	1.15	**2.82**
	± 0.32	**± 0.01**	± 3.75	± 0.06	± 0.56	± 0.01	± 5.42	± 0.04	**± 0.11**

[§] P1 + P21 only. In the case of EXT1 and EXT2, both swelling periods P21* and P22* are simultaneous (Fig. 7 and 8) and therefore only P21* is considered to calculate ΔΦ.